ChemElectroChem

Research Article
doi.org/10.1002/celc.202300110

Chemistry Europe
European Chemical Societies Publishing

www.chemelectrochem.org

Simultaneously Incorporating Atomically Dispersed Co-N_x Sites with Graphitic Carbon Layer-Wrapped Co_9S_8 Nanoparticles for Oxygen Reduction in Acidic Electrolyte

Jun Wu,[a] Mengjun Gong,[a] Wuyi Zhang,[a] Asad Mehmood,[a, b] Jinfeng Zhang,[c] Ghulam Ali,[d] and Anthony Kucernak*[a]

A facile yet robust synthesis is reported herein to simultaneously incorporate atomically dispersed Co-N_x sites with graphitic layer-protected Co_9S_8 nanoparticles (denoted as Co SACs + Co_9S_8) as an efficient electrocatalyst for oxygen reduction in acidic solution. The Co SACs + Co_9S_8 catalyst shows low H_2O_2 selectivity (~5%) with high half-wave potential ($E_{1/2}$) of ~0.78 V_{RHE} in 0.5 M H_2SO_4. The atomic sites of the catalyst were quantified by a nitrite stripping method and the corresponding site density of the catalyst is calculated to be 3.2×10^{18} sites g^{-1}. Besides, we also found the presence of a reasonable amount of Co_9S_8 nanoparticles is beneficial for the oxygen electrocatalysis. Finally, the catalyst was assembled into a membrane electrode assembly (MEA) for evaluating its performance under more practical conditions in proton exchange membrane fuel cell (PEMFC) system.

Introduction

PEMFCs are clean energy conversion devices with high efficiency and are currently undergoing massive deployment, for instance, in the transport sector. The sluggish oxygen reduction reaction (ORR) occurring at the cathode of PEMFCs requires highly active catalysts to promote the commercialization of PEMFCs.[1] So far platinum-group metals (PGMs) have the highest ORR activity and are normally used as the cathode catalysts in PEMFCs.[2] However, the high cost of PGMs account for approximately half of the whole PEMFC stack cost and thus hinder the large-scale application of PEMFCs.[3] This is the main reason why much research effort has been devoted to rational design of efficient lower-cost PGM-free electrocatalysts for ORR. The most promising candidate PGM-free ORR catalysts in acidic medium are the metal-nitrogen doped high surface area carbon materials (M–N-C), within which atomically dispersed transition metal atoms coordinated with nitrogen atoms served as the most active sites.[4] Among all the M–N-C catalysts, Fe-N–C catalysts show the most impressive catalytic performance toward ORR which slowly approaches to that of Pt/C.[5] However, these Fe-N–C catalysts still suffer from poor durability and tend to degrade quickly in the PEMFC environment.[6] Even worse, the dissolved Fe ions from Fe-N–C materials will catalyse radical formation from H_2O_2 via Fenton reactions which are detrimental to fuel cells' durability as the formed hydroxyl radicals degrade the organic ionomers and membranes as shown in Equation (1)[7]

$$Fe^{2+} + H_2O_2 + H^+ \rightarrow Fe^{3+} + OH^{\bullet} + H_2O \qquad \Delta_r G = -20.8\ kJ\,mol^{-1} \tag{1}$$

Where the free energy of the reaction is calculated using the data from.[8]

In comparison, although Cobalt has a Co^{2+}/Co^{3+} redox couple ($E^o_{Co^{3+}/Co^{2+}} = 1.92$ V),[8] the potential of that couple in acid is much higher than that of the iron couple ($E^o_{Fe^{3+}/Fe^{2+}} = 0.772$ V) which means that the corresponding reaction has a positive free energy and so is not spontaneous as seen in Equation (2)

$$Co^{2+} + H_2O_2 + H^+ \rightarrow Co^{3+} + OH^{\bullet} + H_2O \qquad \Delta_r G = +90.0\ kJ\,mol^{-1} \tag{2}$$

Thus Co is not expected to catalyse the formation of hydroxyl radicals under typical operation conditions and there is benefit to consider Co-N–C catalysts. However, Co-N–C catalysts still suffer from unsatisfactory catalytic activity compared with Fe-N–C catalysts, as well as undesirably high H_2O_2 yield produced from the $2e^-$ reduction of oxygen.

To improve the ORR activity of Co-N–C catalysts for PEMFCs, we modified the catalyst preparation based on poly-1,5-

[a] Dr. J. Wu, M. Gong, W. Zhang, Dr. A. Mehmood, Prof. Dr. A. Kucernak
Department of Chemistry
Imperial College London
White City Campus London W12 0BZ (United Kingdom)
E-mail: anthony@imperial.ac.uk
[b] Dr. A. Mehmood
Division 3.6 – Electrochemical Energy Materials, Bundesanstalt für Materialforschung und -prüfung (BAM)
12203 Berlin (Germany)
[c] Prof. J. Zhang
School of Materials Science and Engineering
Tianjin University
Tianjin 300072 (China)
[d] Dr. G. Ali
US-Pakistan Center for Advanced Studies in Energy (USPCASE) Pakistan
National University of Science and Technology (NUST)
H-12, Islamabad, 44000 (Pakistan)

Supporting information for this article is available on the WWW under https://doi.org/10.1002/celc.202300110

Diaminonaphthalene from previous work to synthesize atomically dispersed Co-N_x/C catalyst with graphitic layer-protected Co_9S_8 nanoparticles,[9] which improves the acidic ORR performance with a half-wave potential ($E_{1/2}$) of ~0.78 V_{RHE}, as well as good performance in PEMFC applications.

Results and Discussion

As discussed in the experimental section, catalyst precursors were synthesized in a one pot process at room temperature by dispersing 1,5-diaminonaphthalene, $CoCl_2$, and ammonium persulfate in ethanol and stirring for 22 h. After polymerization and incorporation of $CoCl_2$, the solution was heated up to evaporate the solvent and complete the polymerization. The resulting dry precursors were then pyrolyzed twice as described in experimental section to obtain the target catalysts with high surface area. Aberration-Corrected Transmission Electron Microscope (AC-TEM) was first applied to characterize the microstructure and morphology of the Co SACs + Co_9S_8 catalyst. Figure 1a and b show a typical area on the surface of the Co SACs + Co_9S_8 catalyst where no detectable nanoparticles can be found but a certain amounts of isolated Co atoms were observed uniformly distributed across the carbon matrix. However, as shown in Figure 1c and Figure S1, a number of graphitic layer-wrapped Co_9S_8 nanoparticles with an average particle size of ~20 nm (35 particles analyzed in Figure S1 b) were observed. Figure 1d further revealed the crystal structure of nanoparticles, which corresponds well with the crystal model on the [112] zone axis of Co_9S_8. Additionally, EDS mapping (Figure S2 and Figure 1e) provide further insight into the elemental distribution in this catalyst, which presented homogeneous distribution of Co, N, S and O over the carbon substrate and the Co_9S_8 nanoparticle. Conversely, as shown in the AC-TEM images in Figure S3, only Co single atoms can be found in the Co SACs catalyst with no detectable nanoparticles in the whole catalyst.

XRD was then performed to characterize the crystallinity and any possible phase composition of the as-synthesized catalysts. As shown in Figure 2a, unlike the bare Co SACs catalysts that show\ only two broad peaks attributed to amorphous carbon, the XRD pattern of the Co SACs + Co_9S_8 catalyst contains diffraction peaks located at 15°, 30°, 31°, 47°, and 52° attributed to the (111), (311), (222), (511), and (440) planes of Co_9S_8 (JCPDS 65-6801), respectively, suggesting the formation of Co_9S_8. The trend in graphitization of the carbon matrix was investigated through Raman spectroscopy. The Raman spectra of both the bare Co SACs and Co SACs + Co_9S_8 catalysts are plotted in Figure 2b and fitted to a Lorentzian line shape following the previously reported work where four

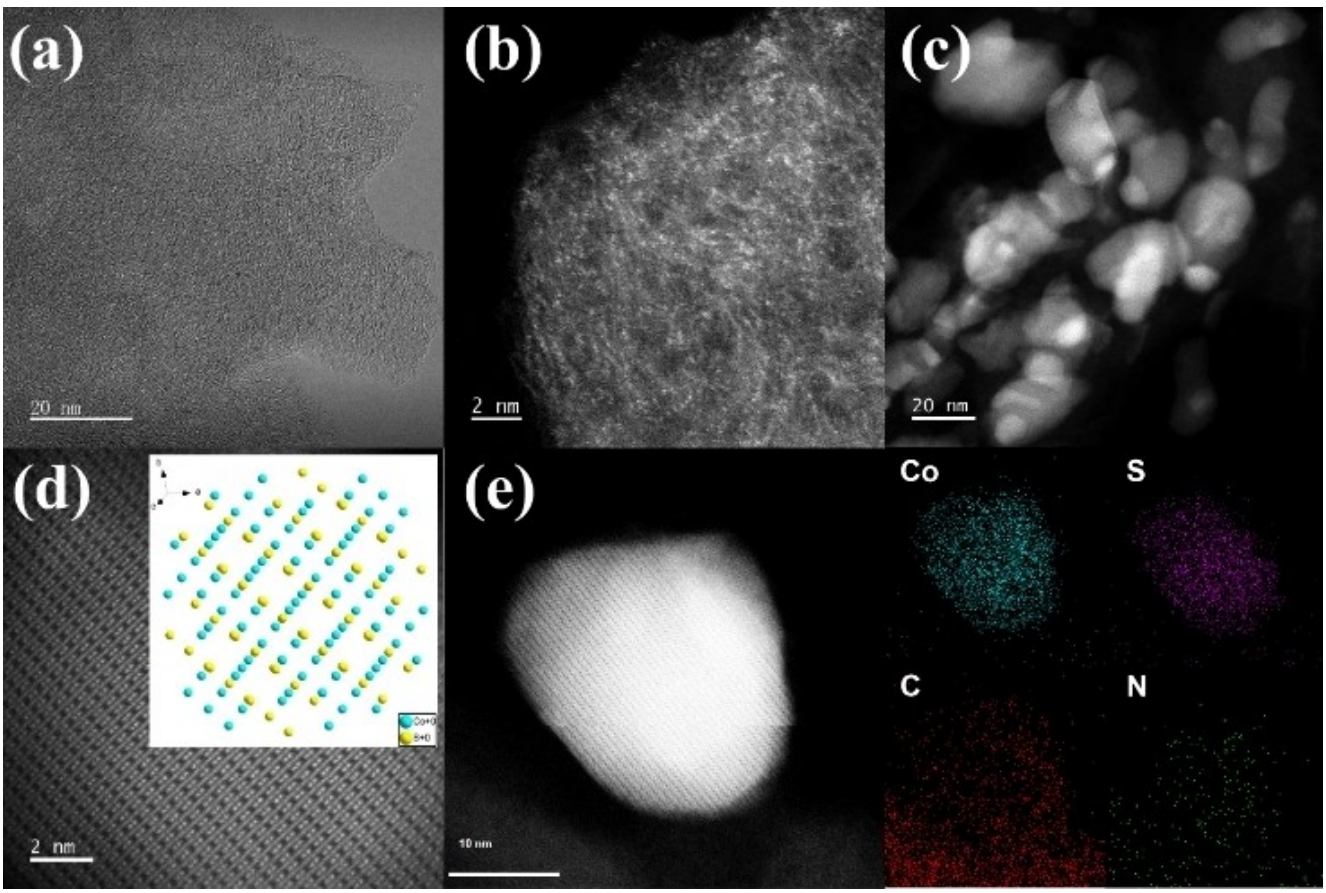

Figure 1. (a) HRTEM image, (b), (c), and (d) HAADF-STEM images of the Co SACs + Co_9S_8 catalyst, the inset is the crystal model on the [112] zone axis of Co_9S_8. (e) EDS mapping of the Co SACs + Co_9S_8 catalyst.

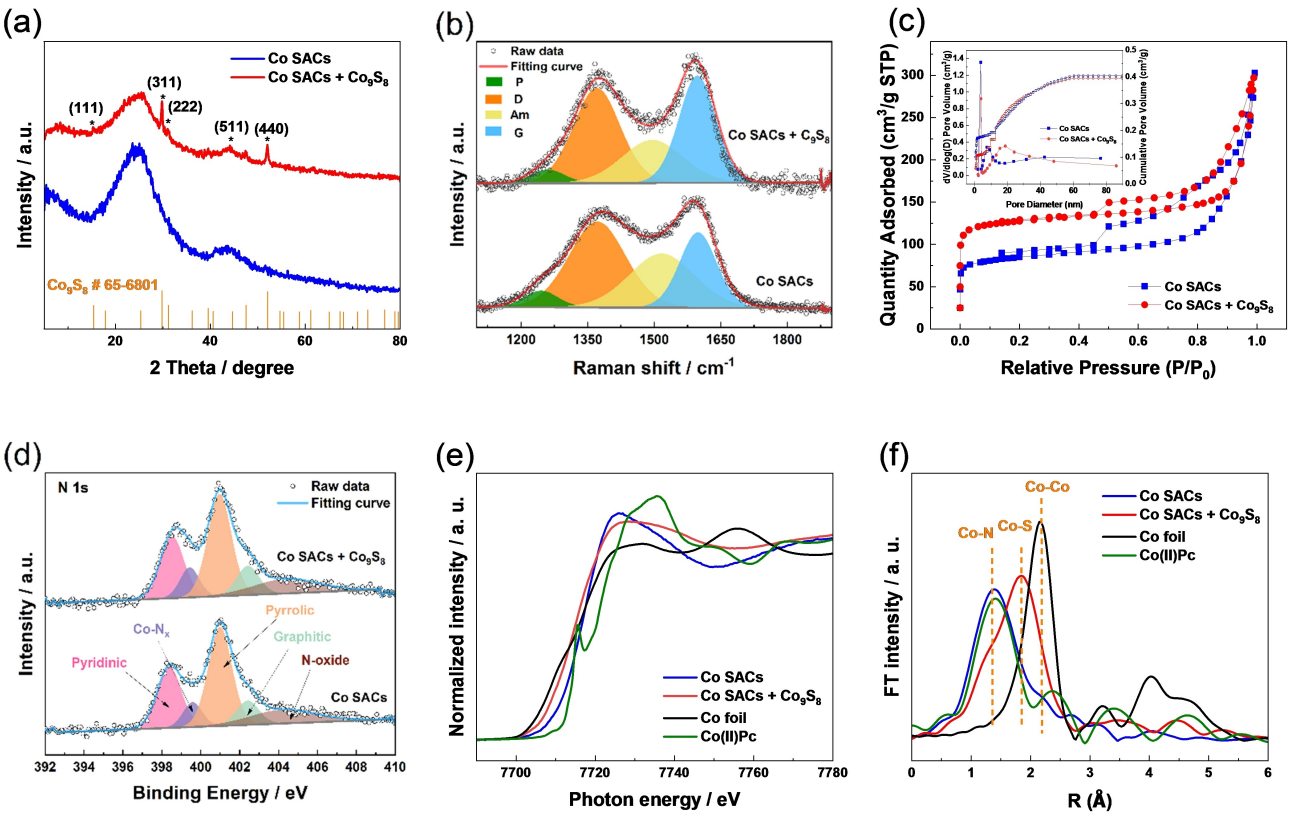

Figure 2. (a) XRD patterns, (b) Raman spectra, (c) N_2 isotherms and corresponding pore size distribution (inset), and (d) High resolution N 1s XPS spectra of the Co SACs and Co SACs + Co_9S_8 catalysts. (e) Co K-edge XANES spectra and (f) Fourier transforms of k^2-weighted Co-K-edge EXAFS spectra of the Co SACs, Co SACs + Co_9S_8, and the reference samples.

symmetric Lorentzian peaks in this region were analyzed, although only two peaks are obvious.[10]

There are two visible peaks: the graphitic G peak (ω_G ~ 1584 cm^{-1}) and the disorder D peak (ω_D ~ 1365 cm^{-1}). The position of the graphitic peak is determined by the number of graphitic planes (n) as seen in Equation (3):

$$\omega_G = 1581.6\frac{11}{(1+n^{1.6})} \quad (3)$$

In our sample we find that the shift in ω_G suggests that there are 5 graphitic layers on average.

Two additional peaks, concealed by the G and D peaks, are properly fitted within the positions of 1490–1525 and 1150–1190 cm^{-1}.[10] The former peak (A_m) is attributed to amorphous carbon while the latter peak is labeled as P and has been proposed to be related to disordered sp^3-bonded carbon.[11] The mean crystallite in plane size of the carbon analyzed, L_a, can thus be calculated as shown in Equation (4)[12]

$$L_a = \frac{560}{E_l^4}\left(\frac{A_G}{A_D}\right) \quad (4)$$

Where E_l is laser energy (eV), and E_l is 2.33 eV for 532 nm, $\left(\frac{A_G}{A_D}\right)$ is the area ratio of G to D.

The average graphene domain size (L_a) of both the bare Co SACs and Co SACs + Co_9S_8 catalysts was thus calculated to be 10.9 nm and 16.9 nm, respectively. Considering the different amount of cobalt resources added in the precursors of these two catalysts, it seems that increasing the metal content during the preparation of the catalysts promotes the formation of larger graphene sheets and the average graphene lengths can be further increased.[13] Moreover, as shown in Figure S4, the Raman spectra in lower wavenumber range of the Co SACs + Co_9S_8 sample shows a distinct vibrational peak at around 665 cm^{-1} together with a set of bands below 750 cm^{-1}, which can be indexed to the characteristic Raman peaks of the Co_9S_8 phase.[14]

The surface areas and porosities of both the bare Co SACs and Co SACs + Co_9S_8 catalysts were examined by nitrogen adsorption. Figure 2c showed the N_2 isotherms and corresponding pore size distribution of the two catalysts. Both catalysts show typical type IV isotherm characteristic of mesoporous materials with a hysteresis loop presenting at high N_2 pressures.[15] As summarized in Table S1, the Brunauer-Emmett-Teller (BET) surface areas of the Co SACs and Co SACs + Co_9S_8 catalysts are 320 and 409 $m^2 g^{-1}$, with microporous surface areas of 228 and 338 $m^2 g^{-1}$, respectively. As has been reported previously the active sites are predominantly hosted in micropores, such large microporous surface areas are expectedly beneficial to the ORR.[16]

Moreover, as summarized in Table S2, the Co SACs + Co_9S_8 showed a slightly smaller average pore size of 4.11 nm compared to that of bare Co SACs (5.85 nm), along with a larger corresponding pore volume of 0.51 $cm^3 g^{-1}$ against that of Co SACs (0.46 $cm^3 g^{-1}$), which are also favorable for heterogeneous oxygen electrocatalysis.[17] In order to understand differences in surface composition, the surface element distribution of the Co SACs and Co SACs + Co_9S_8 catalysts was characterized by XPS. The survey spectrum (Figure S5) revealed small amounts of Co in the Co SACs (~0.15 at%, or 0.69 wt.%) and Co SACs + Co_9S_8 (~0.25 at%, or 1.17 wt.%), as well as the respective N content of 3.94 and 3.35 at% and S content of 0.65 and 0.98 at%. It is clear that the N content decreased while S content increased gradually from the bare Co SACs to the Co SACs + Co_9S_8 catalysts. The decrease in N content might have resulted from the aforementioned formation of more graphitic carbon which can not fix N atoms efficiently compared to disordered carbon.[10,13] The obvious increase in S content should be ascribed to the preferred formation of Co_9S_8 nanoparticles which were surrounded by the graphitic carbon and thus hard to be removed effectively during the acid leaching. Moreover, as shown in the deconvoluted high resolution N 1s spectra (Figure 2d), the N species can be specified into pyridinic-N, Co–Nx moieties, pyrrolic-N, graphitic-N, and N-oxide, which are located at 398.5 eV, 399.4 eV, 400.7 eV, 401.6 eV, and 405.2 eV, respectively.[9,18] Besides, as shown in the S 2p region in Figure S6, the peaks residing at 163.9 eV and 165.2 eV should be associated with the S $2p_{3/2}$ and S $2p_{1/2}$ of C–S–C while the peak at 167.1 eV is marked as SO_x.[19]

Further information for CoN_x coordination and local environment in the bare Co SACs and the Co SACs + Co_9S_8 catalysts was obtained by XAS. As shown in Figure 2e, the near-edge absorption profiles of Co K-edge in both the Co SACs and the Co SACs + Co_9S_8 catalysts are between Co metallic foil and Cobalt (II) phthalocyanine (CoPc), suggesting that the cobalt in these catalysts has an oxidation state between 0 and 2+. Moreover, the corresponding Fourier transforms k^2-weighted phase uncorrected Co K-edge EXAFS for these two catalysts are plotted in Figure 2f. Unlike the Co SACs catalyst which exhibits a prominent peak at ~1.4 Å corresponding to the first coordination shell of CoN_x, the peak of the Co SACs + Co_9S_8 catalyst can be deconvoluted into the Co–N (1.42 Å), Co–S (1.79 Å) and metallic Co–Co (2.17 Å) single scattering paths, respectively, suggesting more complicated coordination environment in this catalyst.[1c,20] The experimental EXAFS spectra for the Co SACs and Co SACs + Co_9S_8 catalysts were properly fitted (Figure S7). The structural parameters, including the average coordination number, bond type and bond length obtained from the fitting, are shown in Table S3. The fitting results show a low average coordination number of ca. 3.1 of the Co SACs catalyst (Co–N2C1), which may suggest the presence of uncoordinated Co cations in this Co SACs catalyst. As for the Co SACs + Co_9S_8 catalysts, the corresponding coordination number of the phase-corrected fitting results' derived bond length for Co–N (~1.89 Å) is 2.8, moreover, the weak signal at ~2.22 Å and ~2.49 Å in this catalysts should be ascribed to the formation of Co_9S_8 nanoparticles wrapped at the graphitic carbon layers, as also evidenced from XRD patterns (Figure 2a) and TEM images (Figure 1c–e and Figure S1).

The ORR activity of the Co SACs, Co SACs + Co_9S_8 catalysts, and the reference Pt/C catalyst in 0.5 M H_2SO_4 is shown in Figure 3a. It can be seen that both the Co SACs and Co SACs + Co_9S_8 catalysts showed reasonable ORR reactivity with the corresponding half-wave potential ($E_{1/2}$) of ~0.73 V_{RHE} and ~0.78 V_{RHE}, as well as the potential of ~0.79 V_{RHE} and ~0.83 V_{RHE} to achieve 10% of limiting current, respectively. The reference Pt/C catalyst showed the highest ORR reactivity with the most positive $E_{1/2}$ of ~0.81 V_{RHE}. The corresponding H_2O_2 yield calculated in Figure 3b on the Co SACs (~8%) is slightly higher than that of the Co SACs + Co_9S_8 catalyst (~5%). Besides, as shown in Figure 3c, the Co SACs + Co_9S_8 catalyst presents a similar Tafel slope of 52.4 $mV dec^{-1}$ compared to that of reference Pt/C (58.6 $mV dec^{-1}$), such a low Tafel slope should be ascribed to surface coverage effects, suggesting that more reaction sites becoming available as the potential is decreased dominates over the acceleration of the reaction with the applied overpotential. Moreover, it has been commonly known that the detected peroxide yield can be affected by the catalyst loading since the thicker catalyst layer under higher catalyst loading may allow further peroxide reduction before it can diffuse out of the catalyst layer if a 2 + 2 mechanism is considered.[21] In this model, two distinct active sites are involved and the initially adsorbed oxygen was firstly reduced to peroxide on one of the active sites. Then the intermediate product peroxide can be further reduced to water on the other active sites.[22] All the active sites might exist in the catalyst at the same time, and if there are enough of the $2e^-$ active sites, a lower catalyst loading will show higher measured peroxide yield at the ring. Therefore, both the Co SACs and Co SACs + Co_9S_8 catalysts were tested under a lower mass loading of 0.2 $mg cm^{-2}$ as shown in the insets of Figure 3a and 3b. It can be clearly seen that for both the Co SACs and Co SACs + Co_9S_8 catalysts the peroxide yield seems to increase under lower catalyst loading, supporting the existence of 2 + 2 dual site ORR mechanism in the catalysts rather than the desirable true 4 electron active sites. As all the catalysts prepared in this work were heat treated twice, it is also interesting to investigate the effect of the 2nd heat treatment step. Both the Co SACs and Co SACs + Co_9S_8 catalysts were prepared with or without the 2nd heat treatment under Argon at 900 °C for 2 hs and their ORR performances were tested under the same conditions. As show in Figure S8, a clear ORR reactivity increase can be seen in both catalysts after the 2nd heat treatment, with a positive shift in half-wave potential of ~50 mV_{RHE} and ~60 mV_{RHE} in the Co SACs and Co SACs + Co_9S_8 catalysts, respectively. Besides, the peroxide selectivity of both the catalysts also showed a moderate decrease compared with the counterparts which had undergone the 2nd heat treatment step. The increase of activity could be attributed to on the one hand the previously mentioned formation of new active sites, due to the metal which has been leached from metallic residual nanoparticles coordinated with nitrogen functionalities, and on the other hand the gasification of unstable sulfur and carbon components formed after the acid treatment and hence improving either

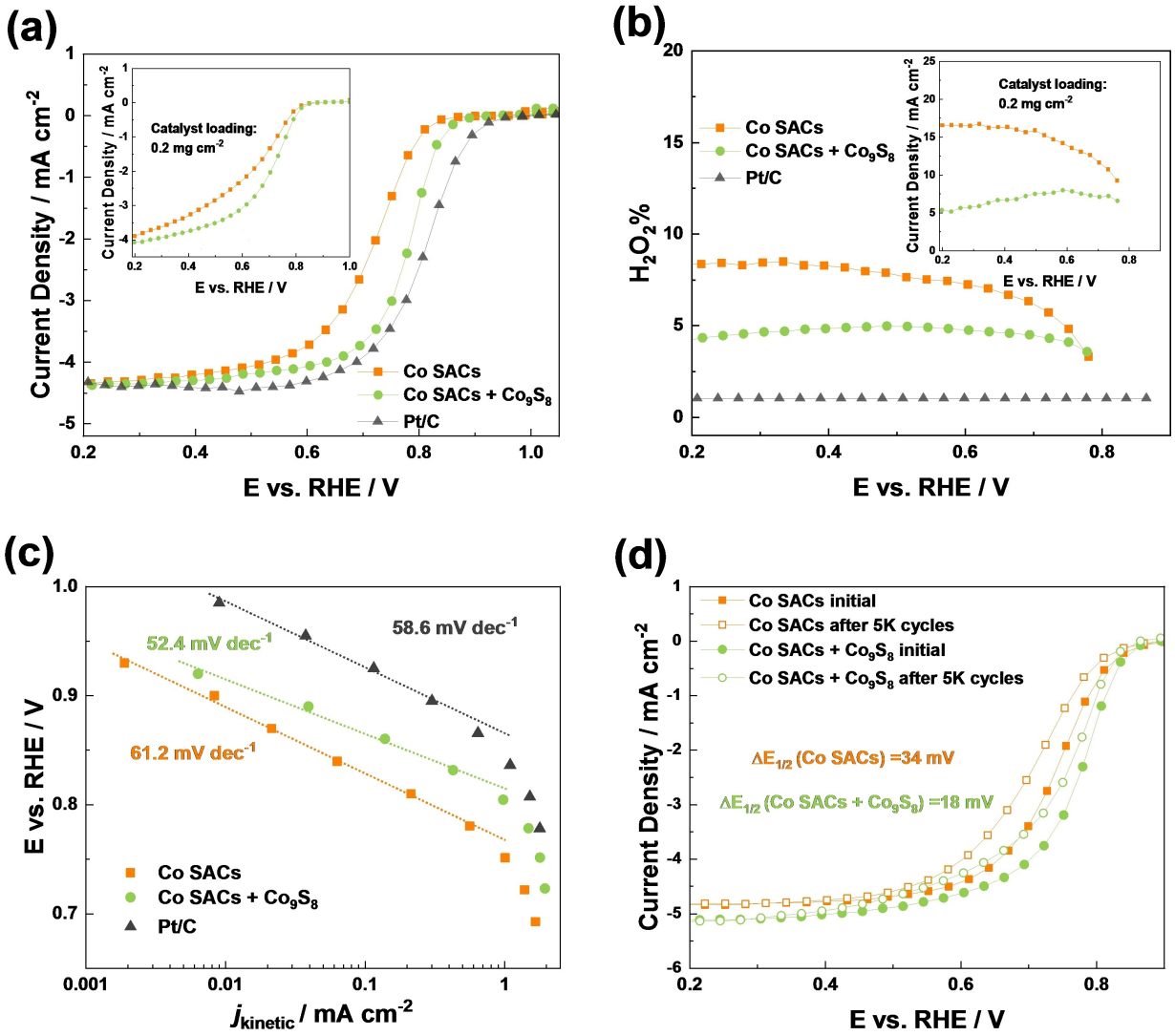

Figure 3. Steady-state RRDE measurements of (a) ORR disk current and (b) H_2O_2 selectivity in 0.5 M H_2SO_4, with Au ring held at +1.5 V_{RHE}, rotating speed: 1600 rpm, 30 s hold, 30 mV step potential, catalysts loading: 0.75 mg cm^{-2}, Pt/C: 20 μg cm^{-2}. (c) Corresponding Tafel slopes of the catalysts for ORR. (d) Steady-state ORR polarization plots of the catalysts before and after 5000 cycling (0.6–1.0 V_{RHE}, O_2-saturated 0.5 M H_2SO_4, 50 mV s^{-1}, 1600 rpm).

mass transport properties or exposing buried metal sites on the surface. Thus, the changes on the surface composition after the 2nd heat treatment were further characterized by XPS. As shown in Figure S9, the 2nd heat treatment did not change the N and Co species significantly but decrease the SO_x species obviously in both the Co SACs and Co SACs + Co_9S_8 catalysts, suggesting surface sulphate species resulted from acid leaching during the synthesis were removed effectively. As further summarized in Table S4 in the XPS survey spectrum, the 2nd heat treatment does not significantly change the amount of N on the surface but increases the content of metal and decreases the S obviously, further confirming the aforementioned assumption about the effect of the 2nd heat treatment. Finally, the cycling stability of both the Co SACs and Co SACs + Co_9S_8 catalysts was compared using RDE measurements. As shown in Figure 3d, after 5000 potential cycles from 0.6 to 1.0 V_{RHE} in an O_2-saturated H_2SO_4 electrolyte, the Co SACs + Co_9S_8 catalyst exhibited a smaller loss in $E_{1/2}$ (18 mV), 16 mV less than that for the bare Co SACs catalyst. Besides, the performance stability of the Co SACs + Co_9S_8 catalyst was also evaluated by a chronoamperometric test on a catalysts coated carbon paper at a fixed disk potential of 0.6 V verse RHE. As shown in Figure S10, the Co SACs + Co_9S_8 catalyst suffered from around 25% loss of its initial ORR current. Moreover, ICP was performed on the electrolyte after 10 h chronoamperometric test but no cobalt species in the solution can be detected. Furthermore, there is no phase change in the XRD pattern (Figure S11a), and no obvious change occurred on the binding energy and component type for Co element in the Co 2p XPS spectrum (Figure S11b) in the post-ORR Co SACs + Co_9S_8 compared to those of the as prepared one, indicating the stability of the Co_9S_8 nanoparticles during acidic ORR. Besides, as shown in Figure S12 and S13, the microstructure and morphology of the post-ORR sample was found out to maintain the original morphology very well after 10 h chronoamperometric test, and the Co_9S_8 nanoparticles could still maintain the same size as

before ORR test. The stability of these nanoparticles under the acidic test environment can be ascribed to the protection of carbon layers.

In order to further quantify the number of Co–Nx sites in the prepared catalystsa series of electrochemical nitrite stripping experiments were performed based on the approach developed by the authors.[23] This nitrite stripping method is based on the selective interaction of Co-N_x sites with probe molecule NO_2^-, which can reversibly bind to the Fe or Co center as nitrosyl at a pH of 5.2 in a 0.5 M acetate buffer. When the catalyst layer has been pre-exposed to nitrite, there is an excess of cathodic charge, Q_{strip}, which can be related to the areal site density (SD) as shown in Equation (5)[23a]

$$SD[site\ nm^{-2}] = \frac{Q_{strip}[Cg^{-1}]^{*}N_A[mol^{-1}]}{n_{strip}F[Cmol^{-1}]^{*}SA[nm^2g^{-1}]} \quad (5)$$

Where n_{strip} is the number of electrons associated with reduction of one adsorbed nitrosyl per site and SA is the surface area of the material. Similarly, the gravimetric site density (MSD), which is the amount of active sites normalized to the mass, can be calculated using Equation (6)[23a]

$$MSD\ [mol\ sites\ g^{-1}] = \frac{Q_{strip}[Cg^{-1}]}{n_{strip}F[C\ mol^{-1}]} \quad (6)$$

Figure 4a shows the ORR performance of the Co SACs + Co_9S_8 catalyst as a function of nitrite poisoning. The catalyst performance is significantly decreased after the adsorption of nitrite intermediate. Most of the activity can be recovered after reductive nitrite stripping but there is a diminution in current at higher overpotential, which might be caused by a time-dependent catalyst degradation or some of the sites being irreversibly poisoned.[1a] Figure S14 shows that all the CVs overlap each other over the potential range where no nitrite reductive stripping occurs. Conversely, when the potential is swept to lower potential in Figure 4b, a clear reductive current appears due to nitrite stripping and this excess current disappears in the following scans. The inset in Figure 4b highlighted the difference between the stripping and recovery curves and the stripping charge can thus be calculated to be 2.55 Cg^{-1}, equal to a MSD value of 3.2×10^{18} sites g^{-1} by Equation (5) and (6). Similarly, the nitrite poisoning experiments were also carried out on the Co SACs catalyst and a smaller MSD value of 0.98×10^{18} sites g^{-1} was obtained (Figure S15). It is interesting to note that the ratio of the accessible metal site densities in the Co

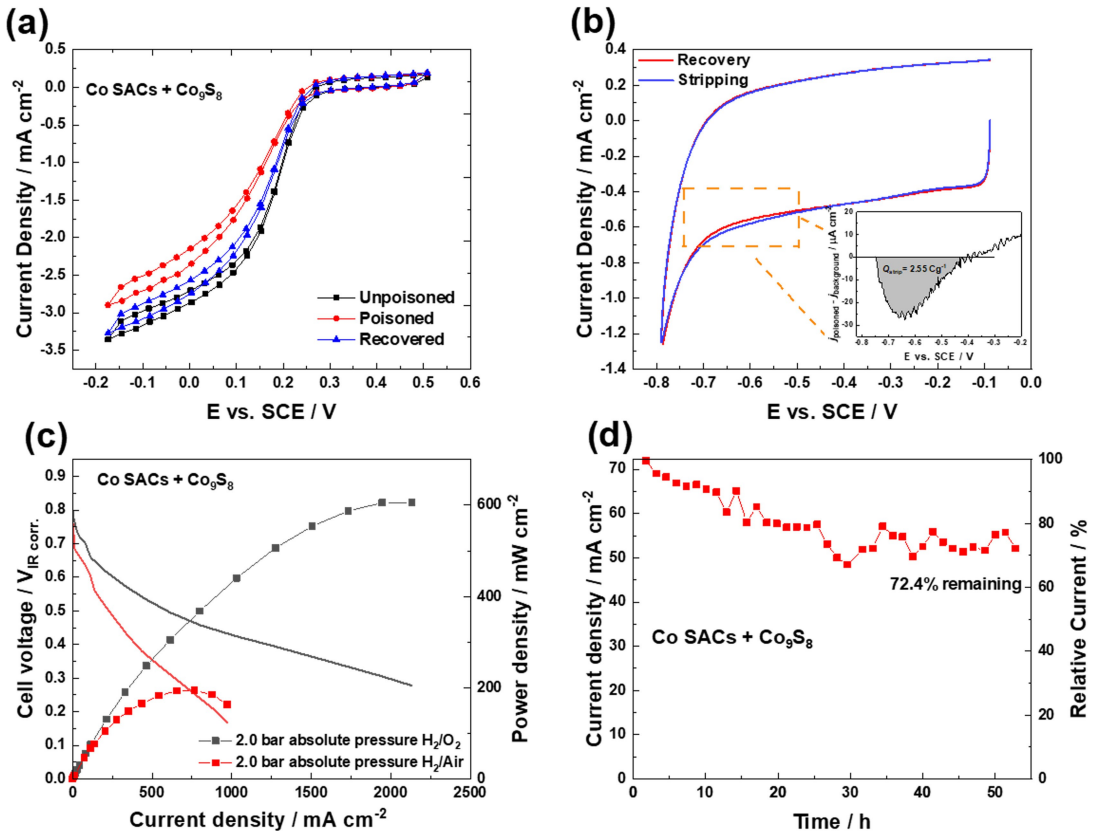

Figure 4. (a) ORR performance of catalyst layer before, during and after nitrite adsorption. (b) Narrow baseline scan in the nitrite reductive stripping region during and after nitrite adsorption. Inset is the stripping charge calculated by subtracting the recovered from poisoned curve in Figure 4b. All experiments were performed in a 0.5 M acetate buffer at pH 5.2 for the Co SACs + Co_9S_8 catalyst using a rotating disk electrode setup: catalyst loading 0.2 mg cm^{-2}. (c) H_2/O_2 and H_2/Air steady-state polarization plot for MEAs comparing a brush painted cathode of the Co SACs + Co_9S_8 catalyst (3.9 mg cm^{-2}) to a commercial Pt anode (0.4 mg_{Pt} cm^{-2}). 80 °C cell temperature. 100% RH and 2 bar absolute pressure gases. (d) Durability tests of the Co SACs + Co_9S_8 catalyst in MEA in 2 bar H_2/Air at a constant cell voltage of 0.6 V with 90% relative humidity on both sides for 50 h.

SACs and Co SACs + Co_9S_8 catalysts is quite close to the amount of metal added during the synthesis. Therefore, it is reasonable to assume that the ORR improvements in the Co SACs + Co_9S_8 catalyst have resulted from on the one hand the increased available metal site densities and on the other hand the formation of reasonable amount of Co_9S_8 nanoparticles, as the strong interaction between such metal nanoparticles and metal-N_x sites has been reported previously to either favor ORR by activating the O–O bond and hence facilitating a direct $4e^-$ process,[24] or induce electron redistribution and modulate electronic configuration of metal-N_x sites.[25] Thus we further prepared Co SACs with higher loading of Co_9S_8 nanoparticles (denoted as Co SACs + HL Co_9S_8) through simply increasing the metal content appropriately during the precursor preparation. The higher ratio of Co_9S_8 nanoparticles to Co SACs in the catalyst was verified by the characterization results shown in Figure S16 and Figure S17. However, as further tested in 0.5 M H_2SO_4 (Figure S18), the ORR performance of the catalyst with higher Co_9S_8 nanoparticles showed even worse ORR performance with an $E_{1/2}$ of ~0.72 V_{RHE}. This suggests that only a reasonable amount of Co_9S_8 nanoparticles along with Co single sites can boost the ORR performance. Although, as shown in Figure S19, the MSD of the Co-N_x sites were also calculated to increase to 8.4×10^{18} sites g^{-1} in this Co SACs + HL Co_9S_8 catalyst. It is worth noting that this MSD of the Co SACs + HL Co_9S_8 catalyst may be overestimated as suggested by the mismatch and the deviation of the baseline scan in the nitrite stripping region during and after nitrite adsorption shown in Figure S19c. Thus, it seems as if the number of single sites in the catalyst does not increase proportionally with the increase of the metal content in the precursor. Nanoparticles (metal sulfide nanoparticles in this synthesis method) will form when the metal content reaches a certain level in the precursor, which makes it difficult to determine how much cobalt exists as single atom and thus correlate it to ORR activity. Besides, higher metal content in the precursor was found to promote the formation of more graphitic carbon and hence reduces its ability to fix nitrogen atoms, which will significantly affect the formation of M-N_x active sites. Moreover, as shown in Figure S16b, the microporous surface area of the catalyst decreased significantly in the presence of more Co_9S_8 nanoparticles, which will also influence the ORR reactivity.

Finally, the best-performing Co SACs + Co_9S_8 catalyst has been tested as the cathode in a PEM fuel cell in order to verify its applicability as fuel cell catalyst. The cathode was prepared by uniformly brush painting the catalyst onto a GDL/MPL at a loading of 3.9 mg cm^{-2} while the commercial Pt anode had a loading of 0.4 mg cm^{-2}. Figure 4c shows both the H_2/O_2 and H_2/Air polarization curves and corresponding power densities. The Co SACs + Co_9S_8 catalyst showed open-circuit voltages (OCV) of 0.797 V and 0.759 V in H_2/O_2 and H_2/Air, respectively. A peak power density of 0.61 W cm^{-2} was achieved in H_2/O_2 tests. Additionally, under H_2/Air conditions, the fuel cell generated a peak power density of 0.25 W cm^{-2}. Although there is still a certain gap in performance between the catalysts prepared in this work and the state-of-the-art Pt/C catalyst under the same conditions. However, as further summarized in Table S6 and S7 compared both the H_2/O_2 and H_2-Air PEMFC performance with the most recent non-Fe PGM-free catalysts reported, our Co SACs + Co_9S_8 catalyst also show the competitive catalytic performance to be used as fuel cell catalyst. Finally, in order to evaluate the durability performance of the catalyst in a real fuel cell condition, 50 h life test at a high operating voltage of 0.6 V was carried out. In addition, for the purpose of minimizing the effect of water flooding issue, the relative humidity is set at 90% although this will cause a slight decrease in initial activity. During the tests, the fuel cell current density at 0.6 V retained 72% of initial activity (Figure 4d), better than most of recently reported Fe-N–C catalysts.[4c,26] The reason for the higher stability of Co SACs + Co_9S_8 catalyst should be ascribed to unfavorable thermodynamics of the formation of radical on Co^{2+} suggested by Equation (1) and 2. Since the radical attack is the one of the reasons for PEMFC performance degradation of Fe-N–C catalysts, the suppressed radical formation on the Co SACs + Co_9S_8 catalyst should be responsible for the relatively high PEMFC stability.

Conclusion

Atomically dispersed Co-N_x sites with graphitic layer-protected Co_9S_8 nanoparticles (denoted as Co SACs + Co_9S_8) and bare Co single atom catalysts were prepared based on the methodology developed in the group where 1,5-diaminonaphthalene is oxidized in the presence of corresponding metal salt with varied metal content in the precursor. The acidic ORR activity of the catalysts was evaluated and the Co SACs + Co_9S_8 catalyst showed a high half-wave potential of ~0.78 V_{RHE}. The catalysts thus carefully characterized physicochemically and electrochemically to investigate the active sites. It was found that the number of single atom sites in the catalyst did not increase proportionally with the increase of the metal content added in the precursor. Nanoparticles (metal sulfide nanoparticles in this synthesis method) were formed when the metal content reached a certain level in the precursor, which made it difficult to determine how much cobalt existed as single atoms and thus correlate it to ORR activity. Besides, higher metal content in the precursor was found to decrease the microporous surface area of the catalyst and promote the formation of more graphitic carbon and hence reduced its ability to fix nitrogen atoms, which significantly affected the formation of M-N_x active sites. Finally, the best Co SACs + Co_9S_8 was assembled into the MEA for evaluating the fuel cell performance and showed reasonable activity and high stability for this type of material.

Supporting Information

The Supporting Information includes high resolution TEM, BET, XRD, XPS, XAS of the Co SACs, Co SACs + Co_9S_8 catalyst, and Co SACs with higher amount of Co_9S_8 catalyst; Steady-state ORR measurements of both the Co SACs and Co SACs + Co_9S_8 catalysts to investigate the catalyst loading effect on peroxide yield and 2nd heat treatment. Nitrite poisoning experiments

quantifying the site density of the Co SACs catalyst. Additional references cited within the Supporting Information.[1c,4a,24a,27]

Experiments and Methods

Synthesis of the Co SACs + Co_9S_8 composite catalysts. 1,5-diaminonaphthalene (1 g, 6.32 mmol, 98%, Alfa Aesar) was firstly dissolved in ethanol (220 mL, absolute VWR). Then a solution of $CoCl_2 \cdot 6H_2O$ (120 mg, 98%, Sigma-Aldrich) was dissolved in ethanol (20 mL, absolute VWR) and sonicated for 10 min and then added to the aforementioned solution. Next, a solution of $(NH_4)_2S_2O_8$ (1 g, 4.38 mmol, 99.9%, Sigma-Aldrich) dissolved in H_2O (10 mL, MilliQ 18.2 MΩ cm) was added after 10 min. The mixed solution was stirred for 22 h and dried under 80 °C to remove the solvent. The remaining precursors were then pyrolyzed in a Carbolite Single Zone tube furnace under 950 °C at a heating rate of 10 °C min^{-1} and held there for 2 h while supplying a constant stream of Ar gas (BIP plus-X47S, Air products). The resulting black powder was then refluxed for 8 h in 0.5 M H_2SO_4 at 110 °C in order to remove residual metal efficiently and then filtered by a polycarbonate (PCTE) membrane filter (0.2 Micron, 47 mm, Sterlitech). The resulting powder was dried at 60 °C and then heat treated for a second time in the tube furnace under Ar with a heating rate of 10 °C min^{-1} and held at 900 °C for 2 h. After cooling down the resulting **Co SACs + Co_9S_8** catalyst was ready to use. The counterpart bare **Co SACs** catalyst was prepared similar to that of the Co SACs + Co_9S_8 catalyst but only 40 mg of $CoCl_2 \cdot 6H_2O$ was added in the precursor. Moreover, in order to investigate the effect of the ratio of Co_9S_8 nanoparticles to Co single atoms in the product, we further prepared the Co SACs with a higher amount of Co_9S_8 nanoparticles catalyst by adding 200 mg of $CoCl_2 \cdot 6H_2O$ to the precursor.

Physical characterization. X-ray diffraction (XRD) was performed on an X-ray diffractometer (Rigaku, Japan) with a Cu-Kα radiation of 0.15418 nm. X-ray photoelectron spectroscopy (XPS) was performed on a Thermo Scientific K-Alpha X-ray Photoelectron Spectrometer system (Al Kα, 1486.6 eV). Transmission electron microscopy (TEM) was performed on a JEM-ARM200F. Raman spectra was obtained on an inVia confocal Raman microscope and a 532 nm laser, Spectra was recorded in the range of 1000–2000 cm^{-1}. N_2 adsorption was performed on an Belsorp-max ASAP 2020 to obtain the Brunauer-Emmett-Teller (BET) surface area. The coordination environment of Co atoms was obtained by X-ray absorption spectroscopy (XAS). The XAS spectra was recorded in fluorescence mode at the 10 C beamline of Pohang Accelerator Laboratory (PAL). Spectra of Co phthalocyanine, Co foil were also measured as reference. XANES and EXAFS spectra were measured to $k = 15$ $Å^{-1}$.[28]

Catalyst ink preparation. The catalyst inks consisted of a known amount of catalyst sonicated with IPA (VWR) and H_2O (MilliQ 18.2 MΩ cm) mixture solution (volume ratio = 1:1) for 30 min. Then Nafion solution (5 wt%, Sigma-Aldrich) following a weight ratio of 0.034 of Nafion to the catalyst was also added. The inks were drop-cast on a glassy carbon disk and dried to achieve a catalyst loading of 0.75 mg cm^{-2}. The reference platinum catalyst was 20 wt% Pt/C from Johnson Matthey (HiSpec 3000).

RRDE measurements. A three-electrode glass cell was used. RHE and glassy carbon rod were used as the reference electrode and the counter electrode, respectively. A potentiostat (Autolab, model PGSTAT302N) was used to control the potential or current during the electrochemical measurements. Steady state ORR polarization curves with iR compensation were obtained under 30 mV step potentials with 30 s hold in O_2-saturated 0.5 M H_2SO_4 (96% Ultrapur from Merck) or 0.1 M KOH (VWR Chemicals, 85.3%). Ultrapure N_2 and O_2 (BIP plus-X47S, Air products) were used to purge the electrolytes. A cleaning protocol was performed firstly before collecting ORR polarization curves which consisted of 20 cycles at 100 mV s^{-1}, 10 mV s^{-1}, and 5 cycles at 5 mV s^{-1} in N_2-saturated electrolyte sequentially in a potential window of 1.05 to −0.2 V_{RHE}. The gold ring in the RRDE was fixed at 1.5 V_{RHE} to detect any hydrogen peroxide generated from $2e^-$ ORR. The percentage of peroxide produced during ORR was calculated using Equation (7)

$$H_2O_2(\%) = \frac{2I_r/N}{I_d + I_r/N} \times 100 \quad (7)$$

where N is the collection efficiency and I_d and I_r are the disk and ring currents, respectively.

RDE nitrite poisoning experiments.[23a] All the nitrite poisoning experiments were performed in a 0.5 M acetate buffer solution at a pH of 5.2 instead of 0.5 M H_2SO_4 in order to exclude the interference of NO_2 formed as a side product during the acid decomposition of nitrite.[23a] After the electrode has undergone a cleaning protocol described in 3.4, a background scan was firstly carried out utilizing the following steps including: (1) Steady state ORR polarization described in 3.4 to measure the performance of the unpoisoned catalyst towards the ORR; (2) A wide potential range from 0.3–1.0 V_{RHE}, avoiding the nitrite reduction area; (3) A narrow potential range from −0.3–0.3 V_{RHE}, in a more reductive region where nitrite reduction occurs. Then the electrode was poisoned in 0.125 M $NaNO_2$ for 300 s under a rotation rate of 300 rpm, followed by washing in DI water for 60 s at 300 rpm. Then the electrode was immersed in 0.5 M acetate buffer solution for another 300 s at 300 rpm, followed by washing in DI water for 60 s at 300 rpm. The aforementioned background scan is then repeated to measure the performance of the catalyst in its poisoned state by nitrite. The adsorbed nitrite can be effectively removed in the last set of scans carried out in the more reductive region. Finally, the background scan was repeated to check that the electrode can be recovered to its initial state. The use of the nitrite stripping method to characterize ORR active sites on Co based catalysts has previously been shown (see Figure S31 in the Supporting Information of reference[23a]).

MEA testing. MEAs were prepared using the Co SACs + Co_9S_8 based cathode and a commercial anode with a loading of 0.4 mg_{Pt} cm^{-2} (Alfa Aesar, Johnson Matthey, Hydrogen Reformate/Cathode). The MEAs were tested in a 850e Fuel Cell Test System (Scribner Associates). Cathode catalyst ink was prepared by mixing the best Co SACs + Co_9S_8 catalyst (20 mg), 5 wt% Nafion® ionomer (20 mg), ultrapure water (260 mg) and isopropanol (540 mg). The ink was sonicated for 1 h and then drop cast onto a gas diffusion layer (GDL, 29 BC, SGL) followed by drying in a vacuum oven at 70 °C for 30 min. The final catalyst loading on the cathode was 3.9 mg cm^{-2}. MEAs were fabricated by hot-pressing the commercial anode and the as-prepared cathode on each side of a Nafion® 211 membrane at 130 °C for 3 min under an applied pressure of 400 kg cm^{-2}. The geometric area of the MEA was 5 cm^{-2} which was installed in a single cell with serpentine type flow field design. The cell temperature was maintained at 80 °C throughout the MEA tests. All gases were fully humidified (100% RH) and 1 bar gauge pressure was maintained at both sides. For the H_2-O_2 tests, the flow rates of both gases were maintained at 200 sccm. For H_2-Air test, flow rates of 300 sccm for hydrogen and 1000 sccm for air were used. Both H_2 and O_2 were of ultrapure grade (BIP Plus, Air products).

Acknowledgements

Jun Wu thanks the China Scholarship Council and Imperial College London for supporting his PhD research. This research has been supported by the U.K. Engineering and Physical Sciences Research Council under project EP/J016454/1.

Conflict of Interests

The authors declare no conflict of interest.

Data Availability Statement

The data used in the production of the figures in this paper are available to download at DOI: 10.5281/zenodo.7915175.

Keywords: Heteroatom Doping · Electrocatalysis · Fuel Cells · Oxygen Reduction · Single Atom Catalysts

[1] a) M. Mazzucato, G. Daniel, A. Mehmood, T. Kosmala, G. Granozzi, A. Kucernak, C. Durante, *Appl. Catal. B* **2021**, *291*, 120068; b) M. Primbs, Y. Sun, A. Roy, D. Malko, A. Mehmood, M.-T. Sougrati, P.-Y. Blanchard, G. Granozzi, T. Kosmala, G. Daniel, P. Atanassov, J. Sharman, C. Durante, A. Kucernak, D. Jones, F. Jaouen, P. Strasser, *Energy Environ. Sci.* **2020**, *13*, 2480–2500; c) X. Xie, C. He, B. Li, Y. He, D. A. Cullen, E. C. Wegener, A. J. Kropf, U. Martinez, Y. Cheng, M. H. Engelhard, *Nat. Catal.* **2020**, *3*, 1044–1054.

[2] a) A. Kongkanand, M. F. Mathias, *J. Phys. Chem. Lett.* **2016**, *7*, 1127–1137; b) S. Ott, A. Orfanidi, H. Schmies, B. Anke, H. N. Nong, J. Hübner, U. Gernert, M. Gliech, M. Lerch, P. Strasser, *Nat. Mater.* **2020**, *19*, 77–85; c) X. Tian, X. Zhao, Y.-Q. Su, L. Wang, H. Wang, D. Dang, B. Chi, H. Liu, E. J. Hensen, X. W. D. Lou, *Science* **2019**, *366*, 850–856.

[3] S. T. Thompson, B. D. James, J. M. Huya-Kouadio, C. Houchins, D. A. DeSantis, R. Ahluwalia, A. R. Wilson, G. Kleen, D. Papageorgopoulos, *J. Power Sources* **2018**, *399*, 304–313.

[4] a) L. Chen, X. Liu, L. Zheng, Y. Li, X. Guo, X. Wan, Q. Liu, J. Shang, J. Shui, *Appl. Catal. B* **2019**, *256*, 117849; b) F. Xiao, G.-L. Xu, C.-J. Sun, M. Xu, W. Wen, Q. Wang, M. Gu, S. Zhu, Y. Li, Z. Wei, *Nano Energy* **2019**, *61*, 60–68; c) N. Zhang, T. Zhou, M. Chen, H. Feng, R. Yuan, W. Yan, Y. Tian, X. Wu, W. Chu, C. Wu, *Energy Environ. Sci.* **2020**, *13*, 111–118; d) A. Mehmood, J. Pampel, G. Ali, H. Y. Ha, F. Ruiz-Zepeda, T. P. Fellinger, *Adv. Energy Mater.* **2018**, *8*, 1701771; e) A. Mehmood, B. Ali, M. Gong, M. G. Kim, J.-Y. Kim, J.-H. Bae, A. Kucernak, Y.-M. Kang, K.-W. Nam, *J. Colloid Interface Sci.* **2021**, *596*, 148–157.

[5] a) J. Wang, Z. Huang, W. Liu, C. Chang, H. Tang, Z. Li, W. Chen, C. Jia, T. Yao, S. Wei, *J. Am. Chem. Soc.* **2017**, *139*, 17281–17284; b) Y. C. Wang, Y. J. Lai, L. Song, Z. Y. Zhou, J. G. Liu, Q. Wang, X. D. Yang, C. Chen, W. Shi, Y. P. Zheng, *Angew. Chem.* **2015**, *127*, 10045–10048; *Angew. Chem. Int. Ed.* **2015**, *54*, 9907–9910; c) A. Mehmood, M. Gong, F. Jaouen, A. Roy, A. Zitolo, A. Khan, M.-T. Sougrati, M. Primbs, A. M. Bonastre, D. Fongalland, G. Drazic, P. Strasser, A. Kucernak, *Nat. Catal.* **2022**, *5*, 311–323; d) D. Menga, J. L. Low, Y. S. Li, I. Arcon, B. Koyuturk, F. Wagner, F. Ruiz-Zepeda, M. Gaberscek, B. Paulus, T. P. Fellinger, *J. Am. Chem. Soc.* **2021**, *143*, 18010–18019.

[6] a) R. Chenitz, U. I. Kramm, M. Lefèvre, V. Glibin, G. Zhang, S. Sun, J.-P. Dodelet, *Energy Environ. Sci.* **2018**, *11*, 365–382; b) C. H. Choi, C. Baldizzone, J. P. Grote, A. K. Schuppert, F. Jaouen, K. J. Mayrhofer, *Angew. Chem. Int. Ed.* **2015**, *54*, 12753–12757; *Angew. Chem.* **2015**, *127*, 12944–12948; c) L. Osmieri, D. A. Cullen, H. T. Chung, R. K. Ahluwalia, K. Neyerlin, *Nano Energy* **2020**, *78*, 105209.

[7] a) L. Gubler, S. M. Dockheer, W. H. Koppenol, *J. Electrochem. Soc.* **2011**, *158*, B755; b) N. Ramaswamy, N. Hakim, S. Mukerjee, *Electrochim. Acta* **2008**, *53*, 3279–3295.

[8] A. Bard, *Standard potentials in aqueous solution*, Routledge, **2017**.

[9] J. Wu, A. Mehmood, G. Zhang, S. Wu, G. Ali, A. Kucernak, *ACS Catal.* **2021**, *11*, 5035–5046.

[10] F. Jaouen, F. Charreteur, J. Dodelet, *J. Electrochem. Soc.* **2006**, *153*, A689.

[11] a) A. Cuesta, P. Dhamelincourt, J. Laureyns, A. Martinez-Alonso, J. D. Tascón, *Carbon* **1994**, *32*, 1523–1532; b) J. Schwan, S. Ulrich, V. Batori, H. Ehrhardt, S. Silva, *J. Appl. Phys.* **1996**, *80*, 440–447; c) R. Shroder, R. Nemanich, J. Glass, *Phys. Rev. B* **1990**, *41*, 3738; d) T. Ungar, J. Gubicza, G. Ribarik, C. Pantea, T. W. Zerda, *Carbon* **2002**, *40*, 929–937.

[12] H. J. Seong, A. L. Boehman, *Energy Fuels* **2013**, *27*, 1613–1624.

[13] D. Malko, T. Lopes, E. Symianakis, A. Kucernak, *J. Mater. Chem. A* **2016**, *4*, 142–152.

[14] a) L.-L. Feng, G.-D. Li, Y. Liu, Y. Wu, H. Chen, Y. Wang, Y.-C. Zou, D. Wang, X. Zou, *ACS Appl. Mater. Interfaces* **2015**, *7*, 980–988; b) X. Lin, Z. Xie, B. Su, M. Zheng, W. Dai, Y. Hou, Z. Ding, W. Lin, Y. Fang, S. Wang, *Nanoscale* **2021**, *13*, 18070–18076.

[15] M. Ferrara, M. Bevilacqua, M. Melchionna, A. Criado, M. Crosera, C. Tavagnacco, F. Vizza, P. Fornasiero, *Electrochim. Acta* **2020**, *364*, 137287.

[16] J.-P. Dodelet, in *Electrocatalysis in fuel cells*, Springer, **2013**, pp. 271–338.

[17] B. Q. Li, C. X. Zhao, J. N. Liu, Q. Zhang, *Adv. Mater.* **2019**, *31*, 1808173.

[18] a) E. Jung, H. Shin, B. H. Lee, V. Efremov, S. Lee, H. S. Lee, J. Kim, W. Hooch Antink, S. Park, K. S. Lee, S. P. Cho, J. S. Yoo, Y. E. Sung, T. Hyeon, *Nat. Mater.* **2020**, *19*, 436–442; b) F. Pan, H. Zhang, K. Liu, D. Cullen, K. More, M. Wang, Z. Feng, G. Wang, G. Wu, Y. Li, *ACS Catal.* **2018**, *8*, 3116–3122.

[19] N. Li, L. Sun, K. Wang, S. Xu, J. Zhang, X. Guo, X. Liu, *J. Energy Chem.* **2020**, *51*, 62–71.

[20] a) Q. Cheng, S. Han, K. Mao, C. Chen, L. Yang, Z. Zou, M. Gu, Z. Hu, H. Yang, *Nano Energy* **2018**, *52*, 485–493; b) Y. Li, R. Cao, L. Li, X. Tang, T. Chu, B. Huang, K. Yuan, Y. Chen, *Small* **2020**, *16*, 1906735.

[21] a) E. J. Biddinger, D. Von Deak, D. Singh, H. Marsh, B. Tan, D. S. Knapke, U. S. Ozkan, *J. Electrochem. Soc.* **2011**, *158*, B402; b) A. Bonakdarpour, M. Lefevre, R. Yang, F. Jaouen, T. Dahn, J.-P. Dodelet, J. Dahn, *Electrochem. Solid-State Lett.* **2008**, *11*, B105.

[22] a) S. Kattel, P. Atanassov, B. Kiefer, *Phys. Chem. Chem. Phys.* **2013**, *15*, 148–153; b) T. S. Olson, S. Pylypenko, J. E. Fulghum, P. Atanassov, *J. Electrochem. Soc.* **2009**, *157*, B54.

[23] a) D. Malko, A. Kucernak, T. Lopes, *Nat. Commun.* **2016**, *7*, 1–7; b) D. Malko, A. Kucernak, T. Lopes, *J. Am. Chem. Soc.* **2016**, *138*, 16056–16068; c) P. Boldrin, D. Malko, A. Mehmood, U. I. Kramm, S. Wagner, S. Paul, N. Weidler, A. Kucernak, *Appl. Catal. B* **2021**, *292*, 120169.

[24] a) X. Cheng, J. Yang, W. Yan, Y. Han, X. Qu, S. Yin, C. Chen, R. Ji, Y. Li, G. Li, *Energy Environ. Sci.* **2021**, *14*, 5958–5967; b) S. H. Yin, J. Yang, Y. Han, G. Li, L. Y. Wan, Y. H. Chen, C. Chen, X. M. Qu, Y. X. Jiang, S. G. Sun, *Angew. Chem.* **2020**, *132*, 22160–22163; *Angew. Chem. Int. Ed.* **2020**, *59*, 21976–21979.

[25] a) J. Chen, B. Huang, R. Cao, L. Li, X. Tang, B. Wu, Y. Wu, T. Hu, K. Yuan, Y. Chen, *Adv. Funct. Mater.* **2023**, *33*, 2209315; b) B. Wu, J. Xiao, L. Li, T. Hu, M. Qiu, D. Lützenkirchen-Hecht, K. Yuan, Y. Chen, *CCS Chemistry* **2023**, 1–12.

[26] a) H. Zhang, S. Ding, S. Hwang, X. Zhao, D. Su, H. Xu, H. Yang, G. Wu, *J. Electrochem. Soc.* **2019**, *166*, F3116; b) X. Zhang, X. Han, Z. Jiang, J. Xu, L. Chen, Y. Xue, A. Nie, Z. Xie, Q. Kuang, L. Zheng, *Nano Energy* **2020**, *71*, 104547.

[27] a) G. P. Hu, C. Chen, H. T. Lu, Y. Wu, C. M. Liu, L. F. Tao, Y. H. Men, G. L. He, K. G. Li, *Engineering* **2020**, *6*, 1364–1380; b) Y. He, S. Hwang, D. A. Cullen, M. A. Uddin, L. Langhorst, B. Li, S. Karakalos, A. J. Kropf, E. C. Wegener, J. Sokolowski, *Energy Environ. Sci.* **2019**, *12*, 250–260; c) J. Liu, X. Wan, S. Liu, X. Liu, L. Zheng, R. Yu, J. Shui, *Adv. Mater.* **2021**, *33*, 2103600; d) R. Wang, P. Zhang, Y. Wang, Y. Wang, K. Zaghib, Z. Zhou, *Prog. Nat. Sci.* **2020**, *30*, 855–860; e) X. X. Wang, D. A. Cullen, Y. T. Pan, S. Hwang, M. Wang, Z. Feng, J. Wang, M. H. Engelhard, H. Zhang, Y. He, *Adv. Mater.* **2018**, *30*, 1706758.

[28] B. Ravel, M. Newville, *J. Synchrotron Radiat.* **2005**, *12*, 537–541.

Manuscript received: March 8, 2023
Revised manuscript received: April 24, 2023
Version of record online: ■■, ■■

RESEARCH ARTICLE

Co_9S_8 nanoparticles, when incorporated with the Co single atom catalysts, provide a synergistic catalyst for oxygen electroreduction in acid solution. Catalysts composed of both components are stable under operating conditions and have been shown to operate well within a fuel cell environment.

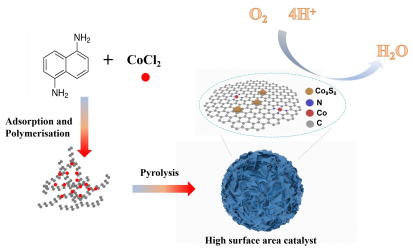

*Dr. J. Wu, M. Gong, W. Zhang, Dr. A. Mehmood, Prof. J. Zhang, Dr. G. Ali, Prof. Dr. A. Kucernak**

1 – 10

Simultaneously Incorporating Atomically Dispersed Co-N_x Sites with Graphitic Carbon Layer-Wrapped Co_9S_8 Nanoparticles for Oxygen Reduction in Acidic Electrolyte